Machine Copy for Proofreading, Vol. x, y–z, 2018

Layer-to-Layer Angle Interlock 3D Woven Bandstop Frequency Selective Surface

Leticia Alonso-González*, Samuel Ver-Hoeye, Miguel Fernández-García, and Fernando Las-Heras

Abstract—A flexible fully textile-integrated bandstop frequency selective surface working at a central frequency of 3.75 GHz and presenting a 0.6 GHz bandwidth has been designed, manufactured and experimentally characterised. The frequency selective surface consists of a multilayered woven fabric whose top layer presents periodic cross-shaped conductive resonators and, due to its symmetries, its performance is largely independent of polarisation and angle of incidence. These properties make the prototype very interesting for shielding applications. The designed frequency selective surface is based on a layer-to-layer angle interlock 3D woven fabric. This technology provides the prototype with flexibility, portability and the possibility of manufacturing it in a large scale production by the use of existing industrial weaving machinery, in contrast to conventional frequency selective surfaces manufactured using rigid substrates. The proposed textile frequency selective surface has been simulated and experimentally validated providing good agreement between the simulations and the measurements. The measured maximum attenuation has been found to be higher than 25 dB under normal incidence conditions.

1. INTRODUCTION

During the last decade, there has been an increasing interest in frequency selective surfaces (FSS) due to the wide number of applications in which they can be employed [1], such as absorbers [2], artificial magnetic conductors [3, 4], electromagnetic shielding, among others. The electromagnetic shielding can be achieved thanks to the bandpass [5, 6] or bandstop [7, 8] responses of the FSS, depending on the design of the periodic structure.

Different approaches have been used to develop FSS, from conventional designs based on resonators implemented over rigid substrates [9–11], FSS based on 3D printing [12], the use of high permittivity ceramic materials in order to avoid conductive materials [13], thicker multiband designs based on substrate integrated waveguide (SIW) technology [14] or multilayered designs [15]. The before mentioned alternatives present different advantages, such as the possibility of achieving high precision details in the fabricated prototypes. Nevertheless, none of them are flexible or washable, and their dimensions are constrained by the prototyping machine or 3D printer, leading to a limited number of unit cells in the manufactured design.

For this reason, during the last few years, there has been an increasing interest in flexible circuits and antennas, based on textile technology, thanks to the possibility of integrating them in special garments and automobile upholsteries, or developing comformable structures for biomedical applications. In the literature, a variety of solutions to develop Textile Integrated Circuits (TIC) has been proposed. Embroidered techniques [16–20], non-woven solutions [21–23], designs based on using several fabrics with different electromagnetic behaviour [24–26] or inkjet printed patterns over textile substrates [27–30] are

Received date: 17 April 2018

* Corresponding author: Leticia Alonso-González (lalonso@tsc.uniovi.es - alonsoleticia@uniovi.es).
The authors are with the Signal Theory and Communications Area, Department of Electrical Engineering, University of Oviedo. Campus Universitario de Viesques, Edificio Polivalente, despacho 0.8.07, Gijón E-33203, Spain.
E-mails: {lalonso, sverhoeye, mfgarcia, flasheras}@tsc.uniovi.es

some of the most cited solutions. More recently, there has been an increasing interest in the development of TIC based on Substrate Integrated Waveguide (SIW) technology [31, 32].

Some of the aforementioned solutions have also been developed to integrate the FSS into the textile. As an example, in [33], a flexible and portable textile-reflectarray backed by an FSS is proposed using two separate embroidered fabrics connected through *Velcros*. However, this solution requires two fabrics and is not appropiate for low profile applications. In [34], an inkjet printed FSS over a fabric is presented, whereas in [35], an FSS is proposed employing the screen printing technology. These procedures present the difficulty of achieving a thin and conductive printed layer over an uneven substrate, leading to the necessity of double-printing the layout or using intermediate impermeable coatings between the fabric and the ink, increasing the number of required subprocesses. Furthermore, the ink must be properly printed on the fabric to avoid its deterioration due to the wear out.

With the aim of pushing textile components to the microwave range, a weaving-based procedure to design, simulate and manufacture RF textile-integrated structures has already been thoroughly discussed in [36–38]. Moreover, this weaving-based procedure presents the advantage of avoiding posterior adhesives, coatings or sewing procedures to manufacture the flexible prototypes. For applications such as momentarily shielding a room from a certain frequency, a flexible woven structure can work as a smart curtain, which is easy to install, uninstall, keep or transport. Moreover, industrial weaving looms allow the automatically manufacturing of very large prototypes, in comparison with standard prototyping machines. For this reason, flexible textile-integrated FSS can overcome the problems attributed to standard FSS, opening a new field of research.

In this paper, a flexible fully textile-integrated bandstop FSS has been designed. It can be manufactured with existing industrial textile machinery, making it suitable for mass production in larger dimensions than conventional FSS based on rigid substrates. The proposed FSS is consists of a layer-to-layer angle interlock 3D woven fabric whose top layer presents periodic cross shaped conductive resonators and its performance is independent of the incident wave direction and polarisation.

The paper is organised as follows. In Section 2, the structure of the FSS will be explained. In Section 3, a description of the employed materials will be presented. In Section 4, the translation into a woven FSS will be discussed. In Section 5, the simulated data will be presented. In Section 6, the fabrication process of the FSS will be explained. In Section 7, the experimental validation will be presented and discussed.

2. STRUCTURE OF THE FSS

A flexible bandstop FSS is proposed to work at 3.75 GHz with a 0.8 GHz bandwidth. The FSS has been designed from a unit cell to which periodic boundary conditions (PBC) have been applied, leading to an ideal infinite FSS. Figure 1a represents an overview of the unit cell and the boundary conditions, as well as a side view of the proposed unit cell where the different layers can be identified. The tangential component of the magnetic field, H_{T}, in the two boundaries which are parallel to the YZ–plane is zero and the tangential component of the electric field, E_{T}, in the two boundaries which are parallel to the XZ–plane is zero, leading to a PBC environment. The unit cell has been iluminated with a plane wave, whose polarisation axis is vertically oriented (Y–axis), propagating in the $\hat{\mathrm{k}}$ direction from port 1 to port 2, so that the S_{21} parameter can be calculated.

The unit cell is composed of three layers, leading to a total height of the unit cell denoted by H. The top layer of the unit cell is composed of a cross-shaped resonator, whose side and width are L_{T} and W_{T}, respectively, as it can be seen on the upper part of Figure 1b. The middle and bottom layers are identical and completely dielectric, as depicted on the bottom part of Figure 1b. The total length of the square-shaped unit cell is L. All the mentioned dimensions are summarised in Table 1.

The proposed FSS is fully integrated in textile, therefore, the conductive and dielectric elements are manufactured using different types of threads. The employed materials will be explained in Section 3 and the translation into a woven prototype will be detailed in Section 4. For this reason, the dimensions summarised in Table 1 have been calculated once a sample of the textile substrate has been electromagnetically characterised, as it will be explained in Section 4.

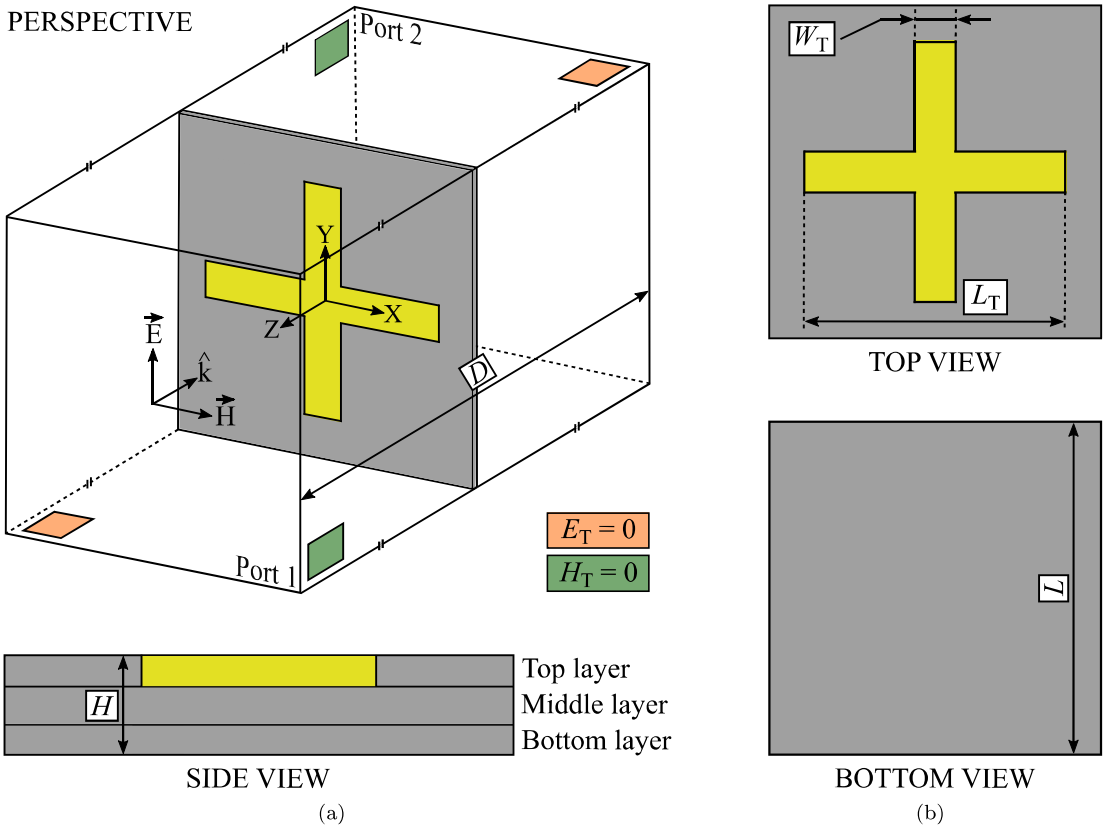

Figure 1. Schematic drawing of the proposed unit cell, conductive materials (yellow) and dielectric materials (grey). The dimensions are summarised in Table 1. (a) Overview of the unit cell with the boundary conditions (D = 1.5 m) and side view of the unit with the notation of the layers. (b) Top and bottom layers of the unit cell and the dimensions.

3. DESCRIPTION OF THE EMPLOYED MATERIALS

Different materials have been employed for the design of the FSS, for both the weft and the warp directions. The weft direction coincides with the width of the fabric and, consequently, with the width of the loom, while the warp direction coincides with the length of the fabric. The warp threads are previously assembled in the loom, whereas the weft yarns are successively inserted in the woven structure during the fabrication process. In the proposed FSS, the warp direction coincides with the direction of the Y–axis. Consequently, the weft direction is oriented in the X–axis direction. In this section, a description of the employed materials and, therefore, the structure of the woven substrate is presented.

Table 1. Dimensions of the top layer and the unit cell of the FSS.

Dimensions (mm)					
Top layer				Unit cell	
L_T	W_T	d_T	s_T	L	H
35	5	0.3	1.2	45	1

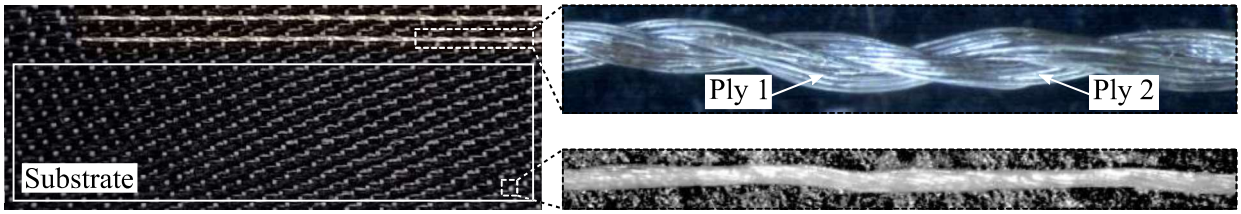

Figure 2. Woven substrate with 2 conductive threads and magnifications: a *Shieldex* thread and a dielectric *PET* warp thread.

3.1. Description of the Electrically Conductive Materials

Electrically conductive *Shieldex 117f17 2-ply* yarns, [39], with a resistance of 3.9 Ω/cm have been used for the conductive warp and weft threads. The ply number means the number of initial threads that are twisted around one another to create a single and stronger thread. These threads consist of two plies and each ply is formed by 17 filaments and weights 117 dtex. The diameter of the *Shieldex 117f17 2-ply* yarns is $d_{\text{Shieldex}} = 0.3$ mm. In the upper right corner of the Figure 2 a sample of a *Shieldex 117f17 2-ply* yarn is depicted.

3.2. Description of the Dielectric Materials

For the dielectric parts of the FSS two different types of threads have been used. For the weft threads, high tenacity black polyethersulfone (commonly known as PES) 550 dtex, formed by 28 filaments, has been employed. The diameter of the *PES* yarns is $d_{\text{PES}} = 0.3$ mm. For the warp threads, white polyethylene-terephthalate (commonly known as PET or polyester) $76f24$, which means that it is composed of 76 filaments with 24 dtex, has been used. The diameter of the *PET* yarns is $d_{\text{PET}} = 0.1$ mm. Figure 2 depicts a sample of the woven substrate, where the black PES is depicted, and a magnification of a warp PET yarn is detailed in the bottom right corner.

4. DESIGN OF THE WOVEN FSS

A layer-to-layer angle interlock 3D woven bandstop FSS is proposed. The FSS has been designed from a unit cell to which PBC has been applied, leading to an ideal infinite FSS. Nevertheless, a finite version composed of 8×8 unit cells has also been simulated to compare the simulations with the measurements. First, a sample of the dielectric substrate has been manufactured and electromagnetically characterised in order to design the FSS and, therefore, translate it into a woven prototype.

The substrate of the FSS is a multilayered fabric composed of three layers of weft *PES* threads interwoven using warp *PET* yarns, leading to a satin woven structure. Due to the air gaps between the threads, a sample of the substrate has been manufactured and electromagnetically characterised using an Agilent Technologies 85072A Split Cylinder Resonator and its relative dielectric permittivity and loss tangent have been found to be $\varepsilon_{\text{subs}} = 1.75$ and $\tan(\delta)_{\text{subs}} = 0.0037$, respectively. Figure 2 represents the top view of a sample of the woven substrate.

As previously mentioned, the woven prototype is composed of three layers: the top layer is a dielectric layer in which the conductive cross-shaped resonators are inserted, and the middle and bottom layers are identical and completely dielectric layers. Two dielectric layers have been employed in order to provide the prototype with more consistency. The three layers are identical, except for the positions where the dielectric threads have been substituted by conductive threads to implement the resonators. The conductive resonators placed in the top layer are translated into 5 *Shieldex* threads as shown in Figure 3a, which will be simulated as 5 conductive strips, separated a distance s_{T} between centres and whose widths are $d_{\text{T}} = d_{\text{Shieldex}}$, as it can be seen in Figure 3b. The middle and bottom layers are completely dielectric as depicted in Figure 3c. The mentioned dimensions are summarised in Table 1.

Nevertheless, Figure 4 depicts different detailed versions of the translation of the unit cell into a woven prototype. Figure 4a represents the detailed uniform cross-shaped resonator which would be structured in a conventional rigid substrate. Figure 4b, Figure 4c and Figure 4d represent, respectively,

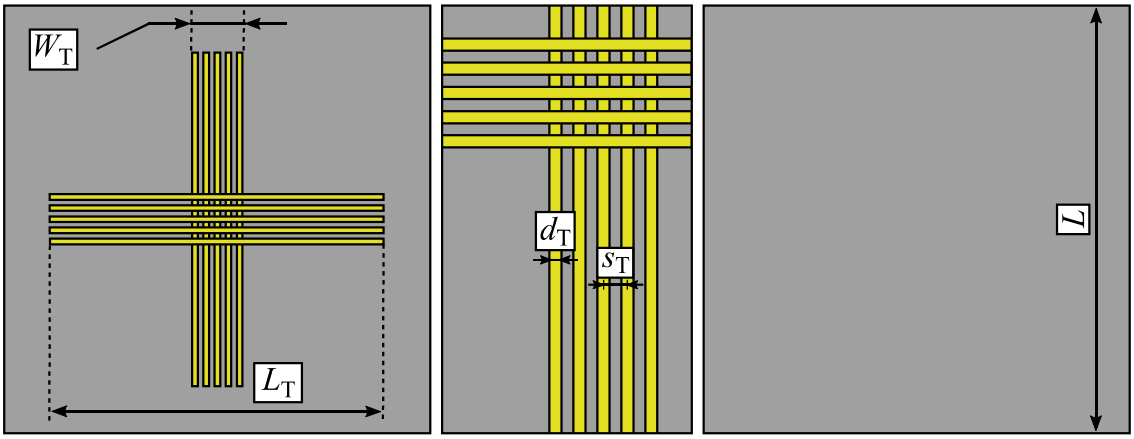

Figure 3. Schematic drawing of the proposed unit cell and its dimensions. The dimensions are summarised in Table 1. (a) Top view. (b) Detailed view of the dimensions (top view). (c) Bottom view.

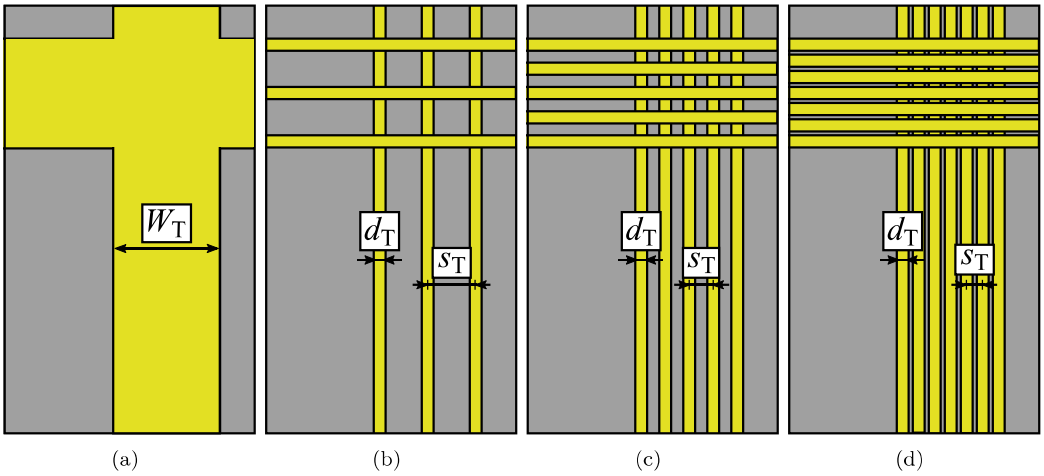

Figure 4. Schematic detailed drawing of the different versions of the proposed unit cell and its dimensions. (a) Uniform . (b) Three strips. (c) Five strips. (d) Nine strips.

a detailed view of the unit cell translated using 3, 5 and 9 strips corresponding to 3, 5 and 9 conductive threads. While the dimension denoted by d_T remains constant in the non-uniform resonators, the distance s_T is modified as summarised in Table 2. In Section 5, the different electromagnetic behaviours of the presented versions is explained.

Table 2. Dimensions of the different versions of the translation into a woven prototype.

Dimensions (mm)							
Figure 4a		Figure 4b		Figure 4c		Figure 4d	
W_T	s_T	d_T	s_T	d_T	s_T	d_T	s_T
5	0	0.3	2.4	0.3	1.2	0.3	0.6

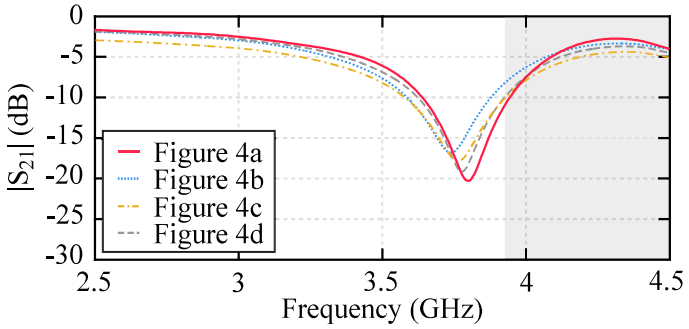

Figure 5. Simulated $|S_{21}|$ parameter for the different versions of the unit cell proposed in Figure 4 using the infinite FSS (set-up in Figure 1a).

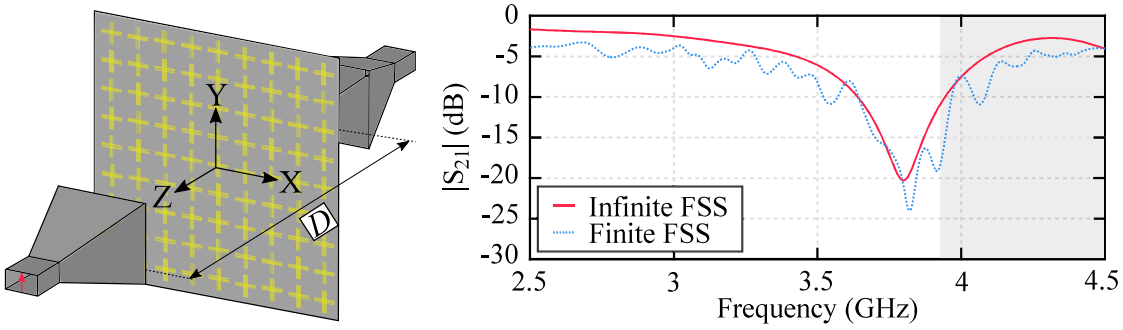

(a) (b)

Figure 6. Normal incidence. (a) Schematic drawing of the simulated set-up ($D = 1.5$ m). (b) Simulated $|S_{21}|$ parameter for an infinite FSS (set-up in Figure 1a) and for a finite FSS in (a).

5. SIMULATIONS

The proposed design has been analysed using the 3D full–wave High Frequency Structure Simulator (HFSS) software. First, different versions of the translation into a woven prototype have been simulated as depicted in Figure 5. These versions have been simulated as infinite FSS using the set-up previously described in Figure 1a. Consequently, the more strips employed in the translation, the higher attenuation achieved. Nevertheless, instead of using the translation proposed in Figure 4d with 9 strips, the translation depicted in Figure 4c with 5 strips has been employed. This decision has been made due to manufacturing specifications.

Then, an infinite FSS modelled as one unit cell (described in Section 4) with PBC has been simulated under normal incidence conditions and the result has been compared with the simulation of a finite structure. Then, the behaviour of the finite FSS in terms of angle of polarisation and angle of incidence has been studied.

An infinite array of resonators has been simulated applying PBC to a unit cell placing two ports at a distance of $D/2 = 0.75$ m from each side of the FSS, respectively, as previously illustrated on the upper part of Figure 1a. A finite version 8×8 unit–cell has also been simulated in the middle between two horn antennas separated a distance D as depicted in Figure 6a. The simulated S_{21} parameter, normalised by the response in the abscence of the FSS, is shown in Figure 6b. The dimensions of the simulated horns are identical to the dimensions of the real horns which have been used for the experimental validation. For this reason, the non-shaded and the shaded range of frequencies represent, respectively, the frequencies in which a single-mode operation of each different horn is guaranteed. This is applicable for the all of the following graphics.

To study the behaviour of the designed FSS in terms of the angle of polarisation, the FSS has been simulated rotating it around its Z–axis, from $\theta = 0°$ to $\theta = 45°$ as depicted in Figure 7a. The simulated

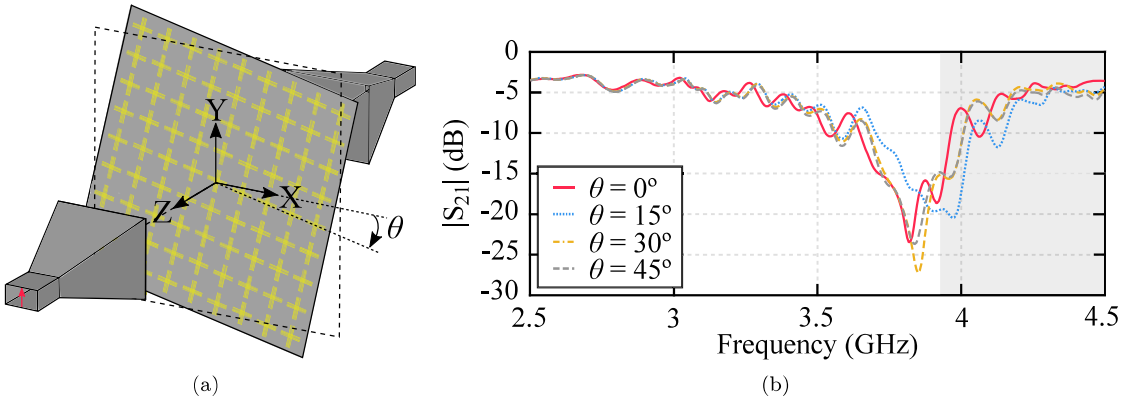

(a) (b)

Figure 7. Angle of polarisation. (a) Schematic drawing of the simulated set-up. (b) Simulated $|S_{21}|$ parameter and the influence of the angle of polarisation on the finite FSS performance.

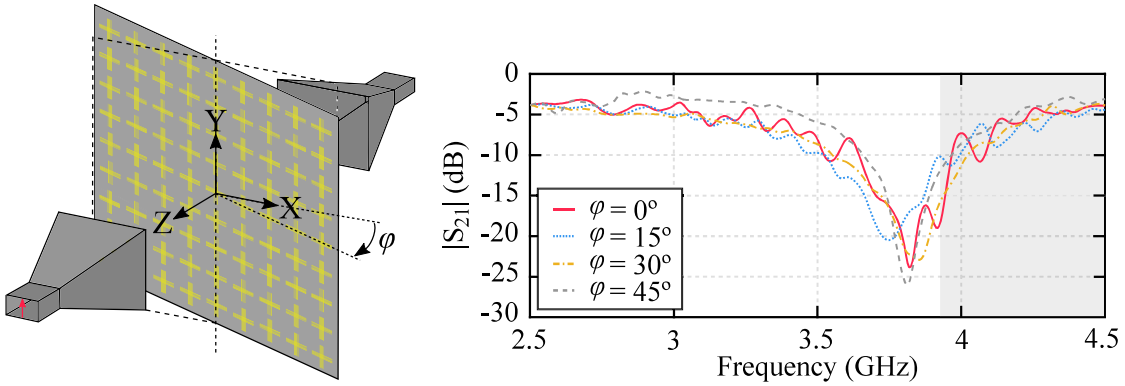

(a) (b)

Figure 8. Angle of incidence. (a) Schematic drawing of the simulated set-up. (b) Simulated $|S_{21}|$ parameter and the influence of the angle of incidence on the finite FSS performance.

$|S_{21}|$ parameter for the different angles of polarisation is shown in Figure 7b. The minimum value of the $|S_{21}|$ parameter is modified with the angle of polarisation, however the attenuation level remains over 10 dB. Consequently, the FSS presents an stable performance in terms of the angle of polarisation.

To study the behaviour of the designed FSS in terms of the angle of incidence, the FSS has been simulated rotating it around its Y–axis, from $\phi = 0°$ to $\phi = 45°$ as depicted in Figure 8a. The simulated $|S_{21}|$ parameter for the different angles of incidence is shown in Figure 8b. Although the minimum value of the $|S_{21}|$ The simulated FSS presents a stable performance in terms of its angle of incidence.

6. FABRICATION PROCESS

A finite 8×8 unit cells FSS has been manufactured using an industrial MüGrip loom. The manufacturing process has been based on satin weaving. The conductive warp yarns are previously mounted in the loom and the conductive weft threads are inserted in the fabric during the fabrication process leading to a conductive lattice in the top layer of the fabric fabric, instead of the required cross-shaped resonators, thanks to an auxiliary layer as depicted in Figure 9a. In Figure 9a, the magenta and blue colored segments of conductive thread correspond, respectively, to the segments of warp and weft conductive threads which are interwoven in the auxiliary layer. In Figure 9b, a schematic drawing of the woven structure after the cutting process is depicted, in which the leftover conductive segments have been removed and the cross-shaped resonators are represented.

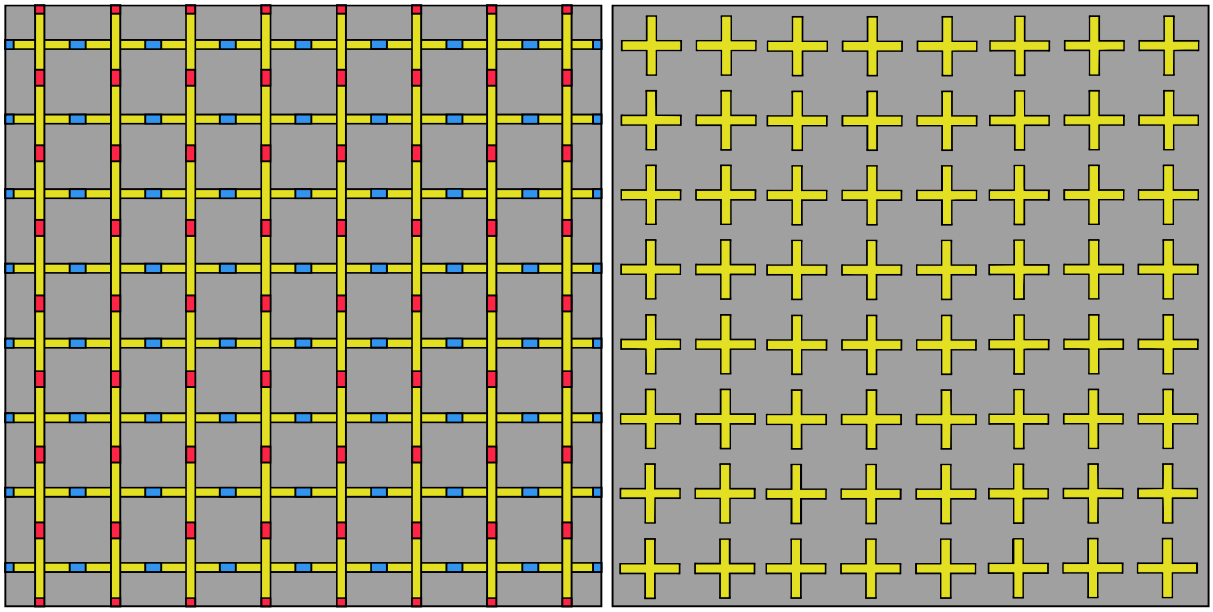

(a) (b)

Figure 9. Schematic drawing of the woven structure before and after the cutting process. (a) Top layer before the cutting process. Magenta and blue colored segments represent, respectively, warp and weft segments of threads which have been left unwoven from the main fabric for the subsequent cutting procedure. (b) Top layer after the cutting process.

With the aim of translating the schematic drawing in Figure 9 into woven patterns, Figure 10 is presented. Figure 10a represents the front view of the weft threads and the side view of the warp patterns. In the segment which corresponds to the separation between two adjacent resonators the conductive threads must be interrupted in order to avoid a shortcircuit. For this reason, during this segment, the conductive warp threads are interwoven in the auxiliary layer and, subsequently, interwoven again in the main fabric. An automatic cutting process is then required to remove the auxiliary layer, leading to the representation despicted in Figure 10b. In this representation, the weft threads corresponding to the positions of the top layer beneath the auxiliary layer have been left loose, after the cutting process.

The described woven patterns lead to a layer-to-layer angle interlock weaving [40–43], due to the individually woven layers of weft threads through undulated warp threads. In order to, not only connect the different layers to create a multilayered structure, but also avoid the presence of loose weft threads after the cutting process, binders must be employed. Binders are threads which, instead of present a woven pattern in an individual layer, they connect different layers to conform a compact woven structure, as depicted in Figure 10c. These threads must be dielectric, in order to achieve the separation between the conductive resonators avoiding the shortcircuits. Due to the necessity of using these binders also between the conductive threads, 5 conductive strips have been employed, instead of 9, in the translation into the woven prototype. By the use of the auxiliary layer and the binders, the different cross-shaped resonators can be achieved as schematically depicted in Figure 10d.

A finishing process is required after removing the fabric from the loom in order to achieve the requirements. Figure 11 depicts a generic finishing process which starts with the insertion of the fabric in liquid chemicals, then needling the fabric and finally applying heat to dry it. The manufactured FSS has been heated at 185° on the frame of the stenter machine.

The top view of the manufacture prototype can be seen in Figure 12a, whereas the bottom view is depicted in Figure 12b. A magnification of a unit cell from the top layer is shown in Figure 12c, whereas its analogous bottom view is depicted in Figure 12d. The white woven lines in the beforementioned figures are due to the binders.

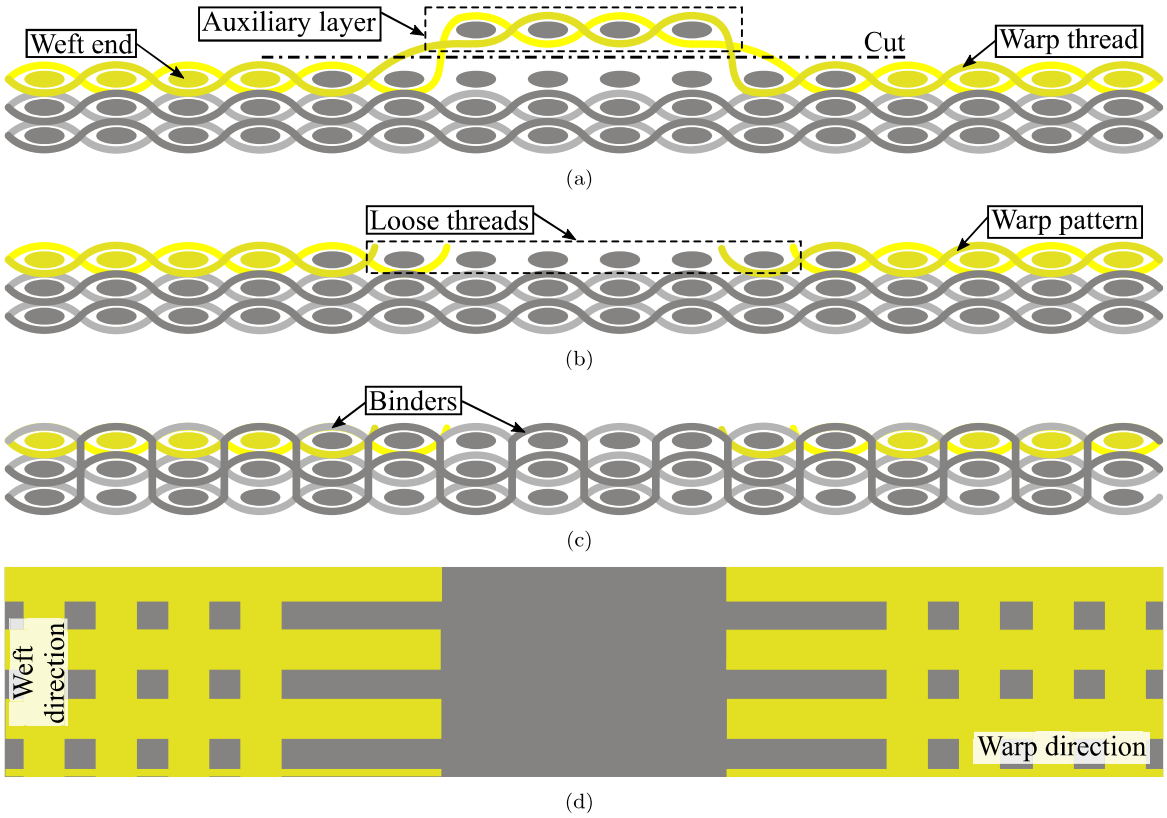

Figure 10. Schematic drawing of the woven structure based on a layer-to-layer angle interlock 3D fabric. (a) Side view of the woven structure with using an auxiliary layer. (b) Side view of the woven structure with the loose threads, after cutting the auxiliary layer. (c) Side view of the woven structure using binders to avoid the loose threads. (d) Top view equivalence.

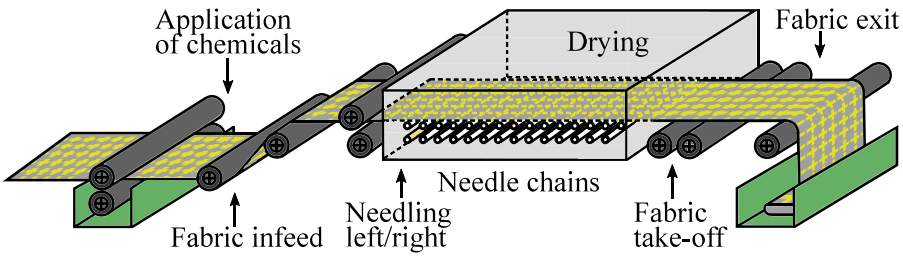

Figure 11. Schematic drawing of the finishing process with a stenter machine.

7. EXPERIMENTAL VALIDATION

The prototype has been experimentally validated using different set-ups and employing two horn antennas, horn #1 and horn #2, respectively, which are depicted in Figure 13, together with their dimensions in centimetres. The horn #1 presents a single-mode operation until a frequency equal to 3.9 GHz, whereas the horn #2 presents its analogous from 3.9 GHz to 5.75 GHz.

All the set-ups are composed of a wooden canvas, in which the prototype has been assembled and allows the required movements for the validation under different angles of incidence, two pairs of horn antennas (for the aforementioned different ranges of frequencies) mounted in rotary platforms for the validation of the different angles of polarisation and a vector network analyser. The S_{21} parameter between the horn antennas, for each set-up, calibrated by using the response between the antennas

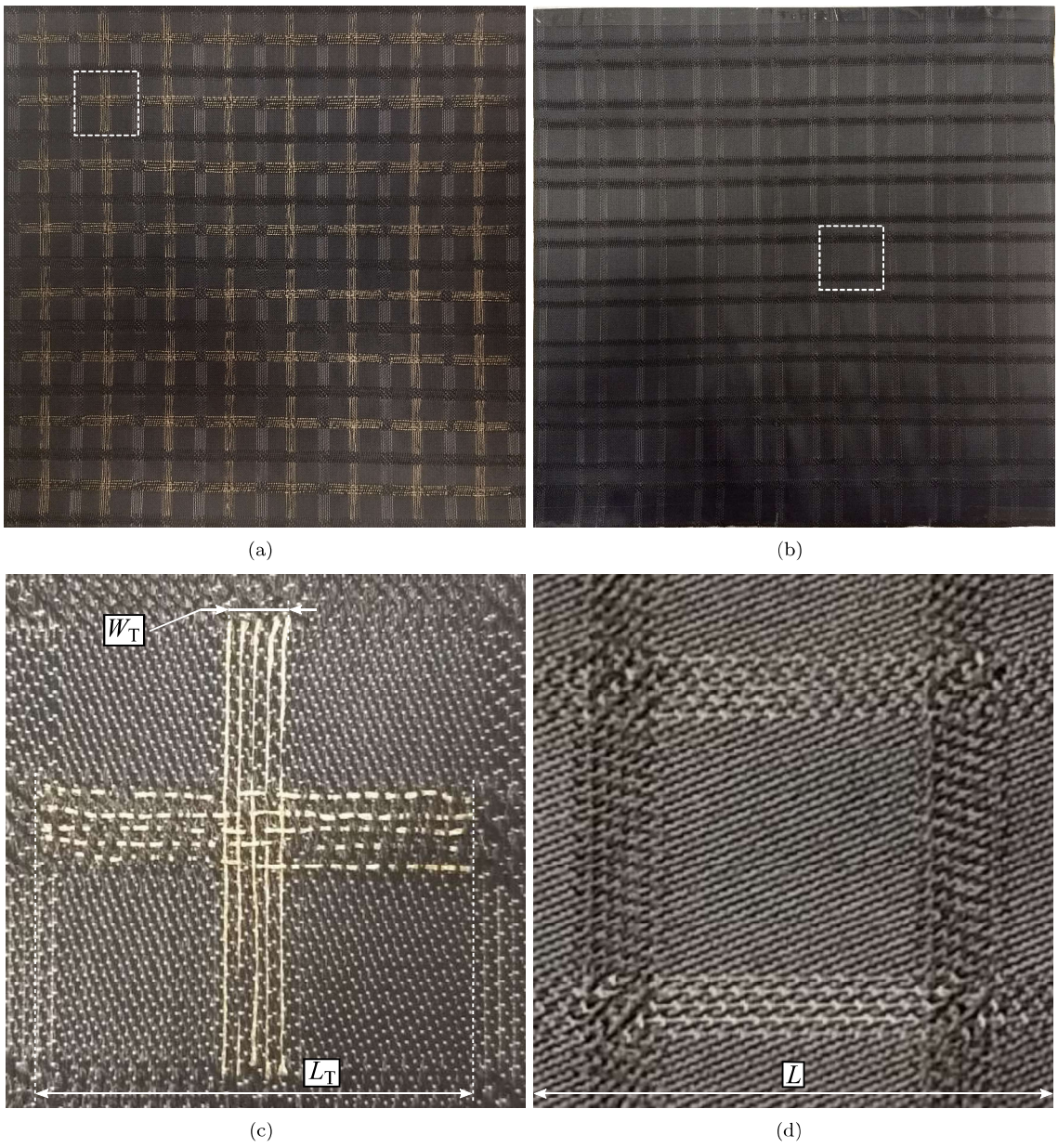

Figure 12. Manufactured prototype and magnification of a unit cell. (a) Top view of the prototype. (b) Bottom view of the prototype. (c) Magnification and dimensions of the top view of the unit cell. (d) Magnification and dimensions of the bottom view of the unit cell.

without the FSS, has been measured using an Agilent N5247A PNA-X vector network analyser and compared with the simulations.

The FSS has been experimentally validated under normal incidence conditions using the set-up shown in Figure 14a. The comparison between simulations and measurements can be seen in Figure 14b. The manufactured FSS provides a bandstop behaviour, $|S_{21}| < -10$ dB, which provides a 0.6 GHz stopband centered at 3.75 GHz, with a 10 dB minimum attenuation and a 27 dB maximum attenuation. The predicted simulated data agree with the measurements, although the differences may be due to the approximations taken into account in the simulations. In the simulations, conductive flat strips are employed for the resonators, whereas the manufactured conductive woven paths are slightly longer due

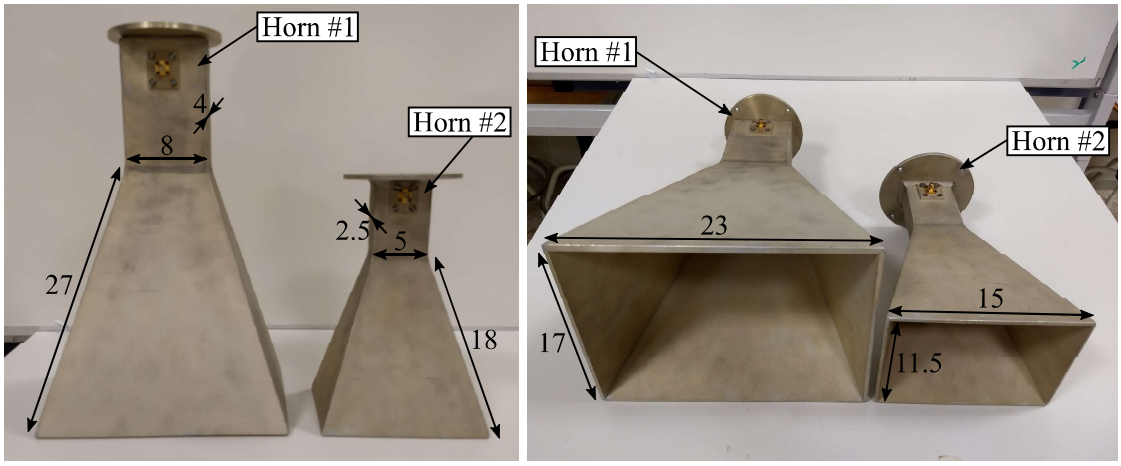

(a) (b)

Figure 13. Horn antennas employed for the measurements and their dimensions in centimetres. (a) Top view. (b) Overview.

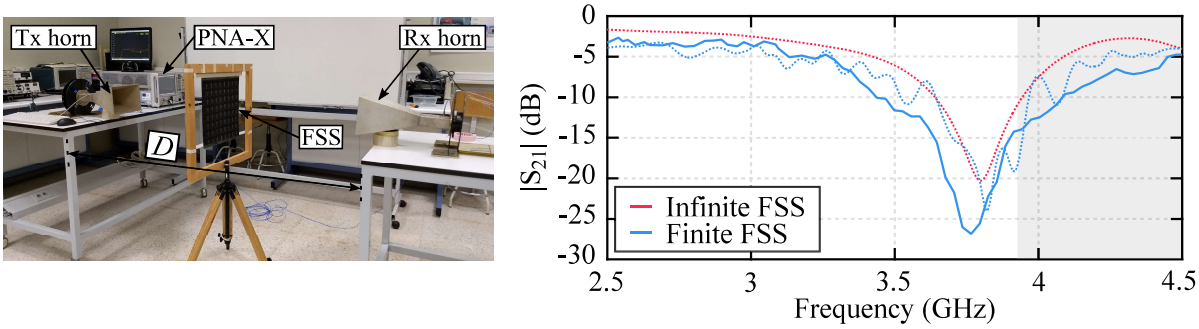

(a) (b)

Figure 14. Normal incidence. (a) Measurement set-up using horn #1 ($D = 1.5$ m). (b) Measured (solid line) vs. simulated (dashed line) $|S_{21}|$ parameter.

to the weaving curves. For this reason, the measured range of working frequencies is slightly lower than the simulated one, although greater.

The FSS has been experimentally validated for different angles of polarisation, $\theta \in [0° - 45°]$, using the set-up shown in Figure 15a in which the antennas have been mounted on the rotary platforms. The comparison between simulations and measurements is depicted in Figure 15b. The manufactured FSS presents a bandstop behaviour, consequently, the FSS exhibits a stable performance in terms of the polarisation angle. This represents an interesting point for the potential use of the proposed FSS as a wall cover to filter undesired frequencies.

The FSS has also been experimentally validated for different angles of incidence, $\phi \in [0° - 45°]$, using the set-up shown in Figure 16a with a rotary canvas. The comparison between simulations and measurements can be seen in Figure 16b. As predicted, the manufactured FSS has a bandstop behaviour. Therefore, the FSS also exhibits a stable performance in terms of the angle of incidence, reinforcing its applicability in the aforementioned wall covering.

8. CONCLUSION

A novel flexible fully textile-integrated bandstop FSS has been presented. A methodology to implement a layer-to-layer angle interlock 3D woven structure and its subsequent cutting procedure to achieve the

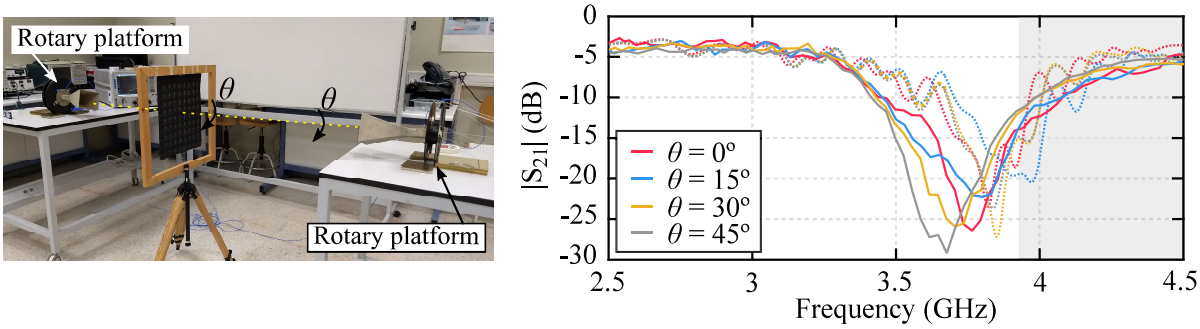

(a) (b)

Figure 15. Angle of polarisation. (a) Measurement set-up using horn #2. (b) Measured (solid line) vs. simulated (dashed line) $|S_{21}|$ parameter and the influence of the angle of polarisation on the finite FSS performance.

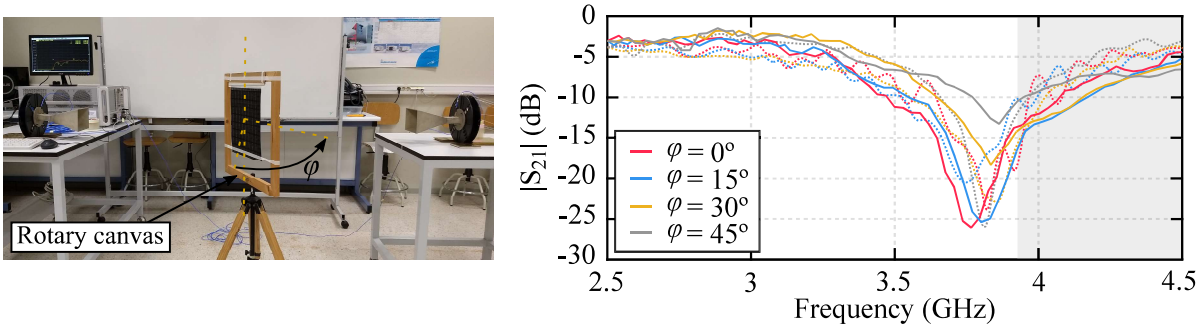

(a) (b)

Figure 16. Angle of incidence. (a) Measurement set-up using horn #2. (b) Measured (solid line) vs. simulated (dashed line) $|S_{21}|$ parameter and the influence of the angle of incidence on the finite FSS performance.

independent resonators have been throughly explained.

To validate the design, a 8×8 unit–cell prototype has been manufactured and experimentally characterised under different conditions, including different angles of polarisation and angles of incidence. A good agreement between simulations and measurements has been achieved, experimentally verifying the theoretically predicted behaviour of the textile structure. Therefore, the manufactured FSS exhibits a stable performance in terms of the angle of polarisation and the angle of incidence.

The manufacturing procedure using industrial textile machinery provides the possibility of manufacturing flexible and large FSS, as opposed to other alternatives based in conventional substrates, solving the fabrication problems of large shielding surfaces.

ACKNOWLEDGMENT

This work has been supported by Gobierno de España TEC2015-72110-EXP, TEC2016-80815-P and FPU14/00016 grant, and by the Gobierno del Principado de Asturias (PCTI)/FEDER-FSE under projects IDI/2016/000372 and IDI/2017/000083.

REFERENCES

1. B. A. Munk, *Frequency selective surfaces: Theory and design.* USA, Wiley-Interscience Publication, 2000, pp. 1-25.

2. J. Tak and J. Choi, "A wearable metamaterial microwave absorber", in *IEEE Antennas Wireless Propag. Lett.*, vol. 16, pp. 784-787, Aug., 2016.
3. S. M. Rouzegar, A. Alighanbari and O. M. Ramahi, "Wideband uniplanar artificial magnetic conductors based on curved coupled microstrip line resonators," in *IEEE Microw. Wirel. Compon. Lett.*, vol. 27, no. 4, pp. 326-328, Apr. 2017.
4. F. M. Monavar and N. Komjani, "Bandwidth enhancement of microstrip patch antenna using Jerusalem Cross-shaped frequency selective surfaces by invasive weed optimization approach," in *Progress In Electromagnetics Research*, vol. 121, pp. 103-120, 2011.
5. J. C. Zhang, Y. Z. Yin, and J. P. Ma, "Design of narrow band-pass frequency selective surfaces for millimeter wave applications," in *Progress In Electromagnetics Research*, vol. 96, pp. 287-298, 2009.
6. W. Fu1 *et al.*, "Polarization insensitive wide-angle triple-band metamaterial bandpass filter", presented in *Progress in Electromagnetic Research Symposium (PIERS)*, Shanghai, China, Aug., 8–11, 2016.
7. C. Xu *et al.*, "A novel dual-stop-band FSS for infrared stealth applications", presented in *Int. Applied Computational Electromagnetics Soc. Symp. (ACES)*, Suzhou, China, Aug., 1–4, 2017.
8. M. Nauman and W. T. Khan, "A miniaturized dual-band stop frequency selective surface for 900 MHz and 1800 MHz bands shielding", presented in *11th European Conf. on Antennas and Propag. (EUCAP)*, Paris, France, Mar., 19–24, 2017.
9. X. Xiong *et al.*, "WiFi band-stop FSS for increased privacy protection in smart building", presented in *IEEE 6th Int. Symp. on Microw. Antenna Propag. and EMC Technol. (MAPE)*, Shanghai, China, Oct., 28–30, 2015, pp. 826-828.
10. N. Liu *et al.*, "A Design Method for Synthesizing Wideband Band-Stop FSS via Its Equivalent Circuit Model", in *IEEE Antennas and Wireless Propag. Lett.*, vol. 16, pp. 2721-2725, Aug., 2017.
11. M. Yan *et al.*, "A novel miniaturized dual-stop-band FSS for Wi-Fi application", presented in *Progress in Electromagnetic Research Symp. (PIERS)*, Shanghai, China, Aug., 8–11, 2016.
12. M. H. Nisanci *et al.*, "Experimental validation of a 3D FSS designed by periodic conductive fibers part-2: band-stop filter characteristic", in *IEEE Trans. on Electromagnetic Compatibility*, vol. 59, no. 6, pp. 1835-1840, Jun. 2017.
13. L. Li *et al.*, "All-dielectric metamaterial band stop frequency selective surface via high-permittivity ceramics", presented in *Progress in Electromagnetic Research Symp. (PIERS)*, Shanghai, China, Aug., 8–11, 2016.
14. W. Fu *et al.*, "Polarization insensitive wide-angle triple-band metamaterial bandpass filter", in *Journal of Physics D: Applied Physics*, vol. 49, no. 28, 2016.
15. M. Fallah, A. Ghayekhloo and A. Abdolali, "Design of frequency selective band stop shield using analytical method", in *Journal of Microw., Optoelectronics and Electromagnetic Applications*, vol. 14, no. 2, Dec. 2015.
16. G. Ginestet *et al.*, "Embroidered Antenna-Microchip Interconnections and Contour Antennas in Passive UHF RFID Textile Tags", *IEEE Antennas Wireless Propag. Lett.*, vol. 16, pp. 1205-1208, Nov. 2017.
17. A. Paraskevopoulos *et al.*, "Higher-mode textile patch antenna with embroidered vias for on-body communication", *IET Microw. Antennas and Propag.*, vol. 10, no. 7, pp. 802-807, May 2016.
18. A. Kiourti, C. Lee and J. L. Volakis, "Fabrication of Textile Antennas and Circuits With 0.1 mm Precision", *IEEE Antennas Wireless Propag. Lett.*, vol. 15, pp. 151-153, May 2016.
19. Z. Wang, L. Zhang, Y. Bayram and J. L. Volakis, "Embroidered Conductive Fibers on Polymer Composite for Conformal Antennas", *IEEE Trans. Antennas Propag.*, vol. 60, no. 9, pp. 4141-4147, Sept. 2012.
20. T. Acti *et al.*, "Embroidered Wire Dipole Antennas Using Novel Copper Yarns", *IEEE Antennas Wireless Propag. Lett.*, vol. 14, pp. 638-641, Nov. 2015.
21. Y. Senbokuya and H. Tsunoda, "A study on the circular patch antennas using conductive non-woven fiber fabrics", presented at IEEE Antennas Propag. Soc. Int. Symp., San Antonio, TX, USA,

June 16–21, 2002.

22. G. Monti, L. Corchia, E. De Benedetto and L. Tarricone, "Wearable logo-antenna for GPSGSM-based tracking systems", IET Microw. Antennas and Propag., vol. 10, no. 12, pp. 1332-1338, Sept. 2016.
23. R. K. Shawl, B. R. Longj, D. H. Werner and A. Gavrin, "The Characterization of Conductive Textile Materials Intended for Radio Frequency Applications", *IEEE Antennas Propag. Mag.*, vol. 49, no. 3, pp. 28-40, June 2007.
24. Xiaoyou Lin, B. C. Seet and F. Joseph, "Fabric antenna with body temperature sensing for BAN applications over 5G wireless systems", presented at the Int. Conf. on Sensing Technol., Auckland, New Zealand, Dec. 8–10, 2015.
25. R. Yahya, M. R. Kamarudin, N. Seman and H. U. Iddi, "Eye shaped fabric antenna for UWB application", presented at the IEEE Antennas Propag. Soc. Int. Symp., Orlando, FL, July 7–13, 2013.
26. H. A. Elmobarak Elobaid, S. K. Abdul Rahim, M. Himdi, X. Castel and M. Abedian Kasgari, "A Transparent and Flexible Polymer-Fabric Tissue UWB Antenna for Future Wireless Networks", *IEEE Antennas Wireless Propag. Lett.*, vol. 16, pp. 1333-1336, Dec. 2016.
27. W. G. Whittow *et al.*, "Inkjet-Printed Microstrip Patch Antennas Realized on Textile for Wearable Applications", *IEEE Antennas Wireless Propag. Lett.*, vol. 13, pp. 71-74, Jan. 2014.
28. A. Chauraya *et al.*, "Inkjet printed dipole antennas on textiles for wearable communications", *IET Microw. Antennas and Propag.*, vol. 7, no. 9, pp. 760-767, June 2013.
29. M. L. Scarpello, I. Kazani, C. Hertleer, H. Rogier and D. Vande Ginste, "Stability and Efficiency of Screen-Printed Wearable and Washable Antennas", *IEEE Antennas Wireless Propag. Lett.*, vol. 11, pp. 838-841, July 2012.
30. M. Akbari, L. Sydänheimo, Y. Rahmat-Sami, J. Virkki and L. Ukkonen, "Implementation and performance evaluation of graphene-based passive UHF RFID textile tags", presented at the Int. Symp. Electromagnetic Theory, Espoo, Finland, Aug. 14–18, 2016.
31. R. Moro, S. Agneessens, H. Rogier, A. Dierck and M. Bozzi, "Textile Microwave Components in Substrate Integrated Waveguide Technology", *IEEE Trans. Microw. Theory Techn.* , vol. 63, no. 2, pp. 422-432, Feb. 2015.
32. F. X. Liu, Z. Xu, D. C. Ranasinghe and C. Fumeaux, "Textile Folded Half-Mode Substrate-Integrated Cavity Antenna", *IEEE Antennas Wireless Propag. Lett.*, vol. 15, pp. 1693-1697, Feb. 2016.
33. M. M. Tahseen and A. A. Kishk, "Flexible and portable textile-reflectarray backed by frequency selective surface", in *IEEE Antennas Wireless Propag. Lett.*, vol. 17, no. 1, pp. 46-49, Jan. 2018.
34. W. G. Whittow *et al.*, "Printed frequency selective surfaces on textiles", in *Electr. Lett.*, vol. 50, no. 13, pp. 916-917, June 19 2014.
35. M. Ghebrebrhan *et al.*, "Textile frequency selective surface", in *IEEE Microw. Wireless Components Lett.*, vol. 27, no. 11, pp. 989-991, Nov. 2017.
36. L. Alonso-González *et al.* "Novel parametric electromagnetic modelling to simulate Textile Integrated Circuits," presented at the Int. Conf. Numerical Electromagnetic and Multiphysics Modeling and Optimization for RF, Microwave, and Terahertz Applications (NEMO), Seville, Spain, May 17–19, 2017.
37. L. Alonso-González *et al.*, "On the techniques to develop millimeter-wave textile integrated waveguides using rigid warp threads", in *IEEE Trans. Microw. Theory and Techn.*, vol. PP, no. 99, pp. 1-11.
38. L. Alonso-González *et al.*, "Fully textile-integrated microstrip-fed slot antenna for dedicated short-range communications", in *IEEE Trans. Antennas Propag.*, doi: 10.1109/TAP.2018.2814203.
39. Shieldex Trading, "Shieldex® Conductive Twisted Yarn Silver Plated Nylon 66 Yarn 117/17 dtex 2-ply," PN# 260121011717, 2010 [Revised Jan. 2012]. [Online]. Available: `www.shopvtechtextiles.com/assets/images/260121011717.pdf`. [Accessed Jan. 21, 2018].
40. B. Yu *et al.*, "2D and 3D imaging of fatigue failure mechanisms of 3D woven composites", in

Composites Part A: Applied Science and Manufacturing, vol. 77, pp. 37-49, Oct. 2015.

41. L. Jin *et al.*, "Tensiontension fatigue behavior of layer-to-layer 3-D angle-interlock woven composites", in *Materials Chemistry and Physics*, vol. 140, pp. 183-190, June 2013.
42. A. C. Long and L. P. Brown, *Composite reinforcements for optimum performance: Modelling the geometry of textile reinforcements for composites: TexGen*, Woodhead Publishing Ltd, 2011, ISBN: 978-1-84569-965-9. [Online]. Available: `www.woodheadpublishing.com/en/book.aspx?bookID=2233`.
43. H. Lin, L. P. Brown, and A. C. Long, "Modelling and simulating textile structures using TexGen" in *Advanced Materials Research*, vol. 331, 2011.